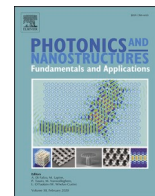


Contents lists available at [ScienceDirect](https://www.sciencedirect.com)

Photonics and Nanostructures - Fundamentals and Applications

journal homepage: www.elsevier.com/locate/photonics

Optimized, highly efficient silicon antennas for optical phased arrays

Henna Farheen^a, Andreas Strauch^a, J. Christoph Scheytt^b, Viktor Myroshnychenko^a, Jens Förstner^{a,*}

^a Department of Theoretical Electrical Engineering, Paderborn University, Warburger Street 100, 33098 Paderborn, Germany

^b Department of System and Circuit Technology, Paderborn University, Fürstenallee 11, 33102 Paderborn, Germany

ARTICLE INFO

Keywords:

Antennas
Phased arrays
Field of view
Directivity

ABSTRACT

Silicon photonics, in conjunction with complementary metal-oxide-semiconductor (CMOS) fabrication, has greatly enhanced the development of integrated optical phased arrays. This facilitates a dynamic control of light in a compact form factor that enables the synthesis of arbitrary complex wavefronts in the infrared spectrum. We numerically demonstrate a large-scale two-dimensional silicon-based optical phased array (OPA) composed of nanoantennas with circular gratings that are balanced in power and aligned in phase, required for producing elegant radiation patterns in the far-field. For a wavelength of 1.55 μm , we optimize two antennas for the OPA exhibiting an upward radiation efficiency as high as 90%, with almost 6.8% of optical power concentrated in the field of view. Additionally, we believe that the proposed OPAs can be easily fabricated and would have the ability to generate complex holographic images, rendering them an attractive candidate for a wide range of applications like LiDAR sensors, optical trapping, optogenetic stimulation, and augmented-reality displays.

1. Introduction

Phased arrays are devices that consist of multiple receiving or transmitting antennas [1], where manipulation of amplitude and phase of each antenna element can be used to control the shape and direction of radiation field from the array, utilizing constructive and destructive interference [2]. For decades, the radio-frequency phased arrays were rigorously investigated and extensively employed in a variety of applications going from the radar to broadcasting applications [3]. Their optical counterparts are also attractive, which offer on-chip integration of thousands of elements for short optical wavelengths of interest at a much lower cost and form factor [4]. These optical analogs are versatile devices that could be utilized for several applications like free-space communication [5,6], optical switches [7], holographic displays [8], and light detection and ranging (LiDAR) [9–12].

Several demonstrations have been made to realize OPAs in integrated photonic platforms like indium phosphide [13], silicon nitride [14], III/V hybrid platforms [15,16], liquid crystals [17], etc. [18]. However, a promising platform to furnish high-yield, cost-efficient commercial systems is silicon photonics, which is highly compatible with the standard CMOS technology [19]. This is commonly accomplished using the silicon-on-insulator (SOI) process, where the top silicon layer realizes all the active and passive components of the array like

the directional couplers, phase shifters, waveguides, and optical antennas [20]. A plethora of optical phased arrays (OPAs) have already been developed using this combination [21–23].

Silicon photonics makes it possible to reliably integrate a large number of densely packed microelectronics. However, the number of these elements and the spacing between them can be used to tailor the angular resolution, beamwidth, grating-lobe spacing, and power of the emission pattern [24]. In particular, a high resolution can be obtained by increasing the number of optical antennas, but on the other hand, their large size results in an inter-element spacing that is larger than the optical wavelength λ [4]. As a consequence, an increased number of grating lobes appear undesirably, which limits the field of view (FOV) of the OPA and, in turn, its grating-lobe-free steering range [25]. In this regard, 1-D beam steering has been demonstrated with 1-D OPAs that can tightly assemble long and narrow radiators [26–28]. These systems are capable of steering the beam in one direction only, unless utilized with a highly precise tunable laser, making 2-D beam steering possible [29]. Furthermore, 2-D beam steering has also been shown by dispersive OPAs [30], circular OPAs [31], and planar OPAs [32].

In this work, we aim to improve the efficiency in the FOV for the OPA presented in [32]. In particular, we use full-wave numerical simulations in conjunction with a hybrid optimization routine that employs particle swarm and trust-region optimization to increase the amount of power

* Corresponding author.

E-mail address: jens.foerstner@uni-paderborn.de (J. Förstner).

<https://doi.org/10.1016/j.photonics.2023.101207>

Available online 28 November 2023

1569-4410/© 2023 The Author(s). Published by Elsevier B.V. This is an open access article under the CC BY license (<http://creativecommons.org/licenses/by/4.0/>).

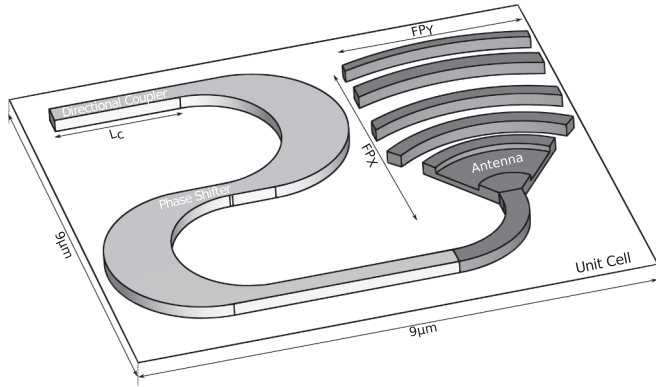


Fig. 1. Schematic representation of the $9 \mu\text{m} \times 9 \mu\text{m}$ unit cell. The three main components include the direction coupler, phase shifter, and dielectric antenna. The parameters FP_x and FP_y represent the footprint of the antenna along the x - and y - coordinates, respectively. The dark gray region shows the component optimized in this work.

directed by the dielectric nanoantenna from a unit cell into the FOV of the array [33–35]. Our optimized antenna directs almost 5 times more power into the FOV than the reference antenna. Furthermore, we propose a modified structure that can further enhance this power to 10 folds by using a simple, yet efficient Bragg reflector made of silicon. We anticipate that our optimized antennas can be easily fabricated and utilized for enhancing the performance of LiDAR and OPAs used in different applications.

2. Numerical setup

In this work, we optimize the emission characteristics of two different antennas that can be used in a two-dimensional OPA. Each unit

cell of the OPA comprises three main components, namely, a directional coupler (DC), phase shifter (PS), and a low-loss dielectric antenna, as shown in Fig. 1. The technical specifications of the DC and PS were taken into consideration for defining the footprint constraints in the optimization of the antenna component to fit it exactly in the same compact footprint of $9 \mu\text{m} \times 9 \mu\text{m}$ as the original design in [32]. The antennas are made of silicon with a refractive index of $n_{\text{Si}} = 3.48$ and are simulated in a silicon-dioxide cladding having a refractive index of $n_{\text{SiO}_2} = 1.45$. The large refractive index contrast between the two materials facilitates a stronger light-matter interaction. Fig. 2a and Fig. 3a show the schematic representation of the antennas, which are oriented along the xy -plane with a direction of propagation along the x -axis. These antennas are excited with the fundamental transverse electric (TE) mode at an operational wavelength of $1.55 \mu\text{m}$. Full-wave numerical simulations were performed using CST Microwave Studio in the frequency domain utilizing the finite element method [36]. The computational domain of the simulations is surrounded by an open boundary in which the far-field for the antenna is obtained using near-to-far-field transformation utilizing the fields at the bounding box of the simulation domain [37]. The optimization utilized the particle swarm algorithm, a heuristic global optimizer in conjunction with the trust-region method, a local optimization technique. This hybrid optimization routine requires more iterations in comparison to other techniques such as topological optimization, that in addition, are not constrained by a pre-defined starting structure [38]. However, the proposed routine has a higher probability of finding a global optimum with high accuracy due to a thorough examination of the search space. This numerical setup works with a large number of parameters providing more degrees of freedom, while also accounting for variations in the antenna geometries. We optimize the power efficiency of the antenna in the FOV, i.e., the grating-lobe-free region that along θ_x and θ_y can be defined as [19,39]

$$-\sin^{-1}\left(\frac{\lambda_n}{2d}\right) < \Delta\text{FOV} < \sin^{-1}\left(\frac{\lambda_n}{2d}\right), \quad (1)$$

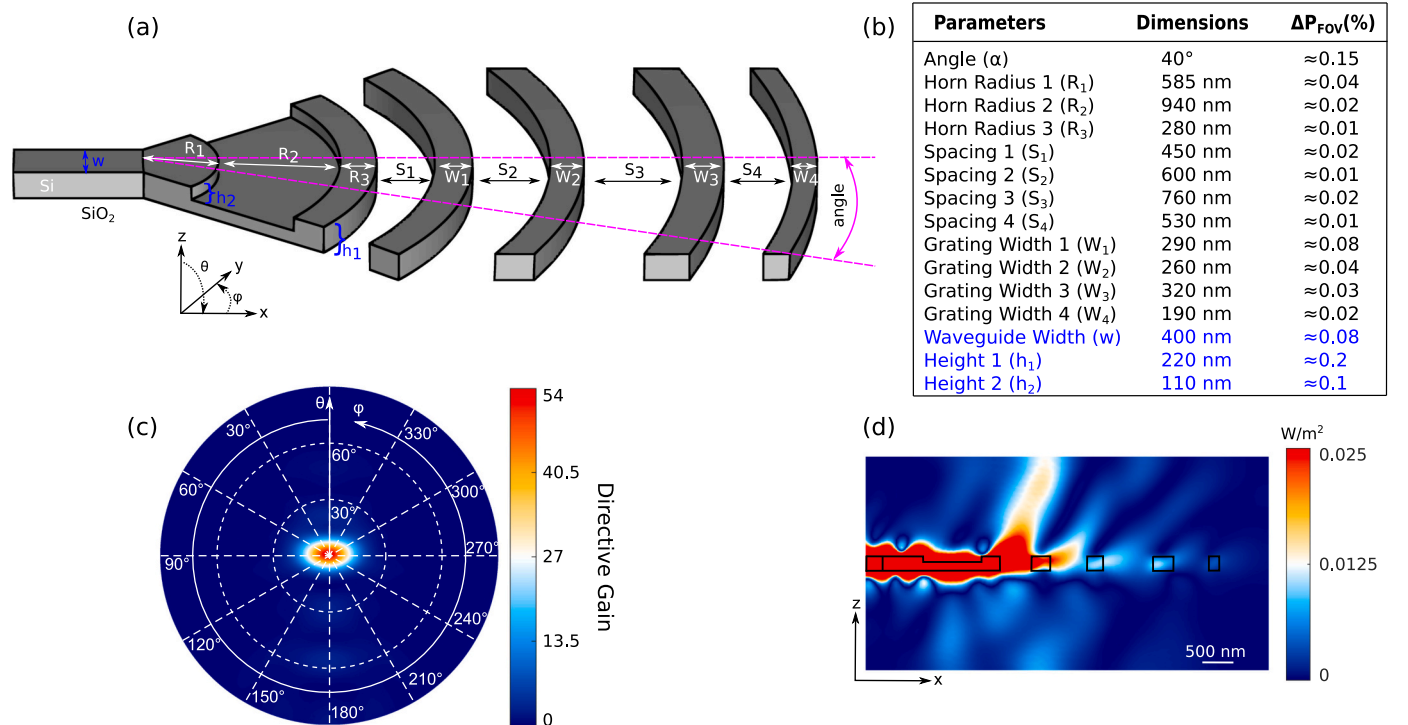


Fig. 2. (a) Schematic representation of the dielectric antenna optimized for $1.55 \mu\text{m}$, highlighting the parameters used in the optimization. (b) Design parameters obtained for the optimized antenna. The parameters depicted in blue were fixed as constant values. (c) Calculated angular linear directive gain distribution of the optimized antenna exhibiting a directivity of $D = 54$ at $\theta = 0^\circ$. (d) Calculated near-field distribution of the power flow of the optimized antenna in the xz -plane at $y = 0$.

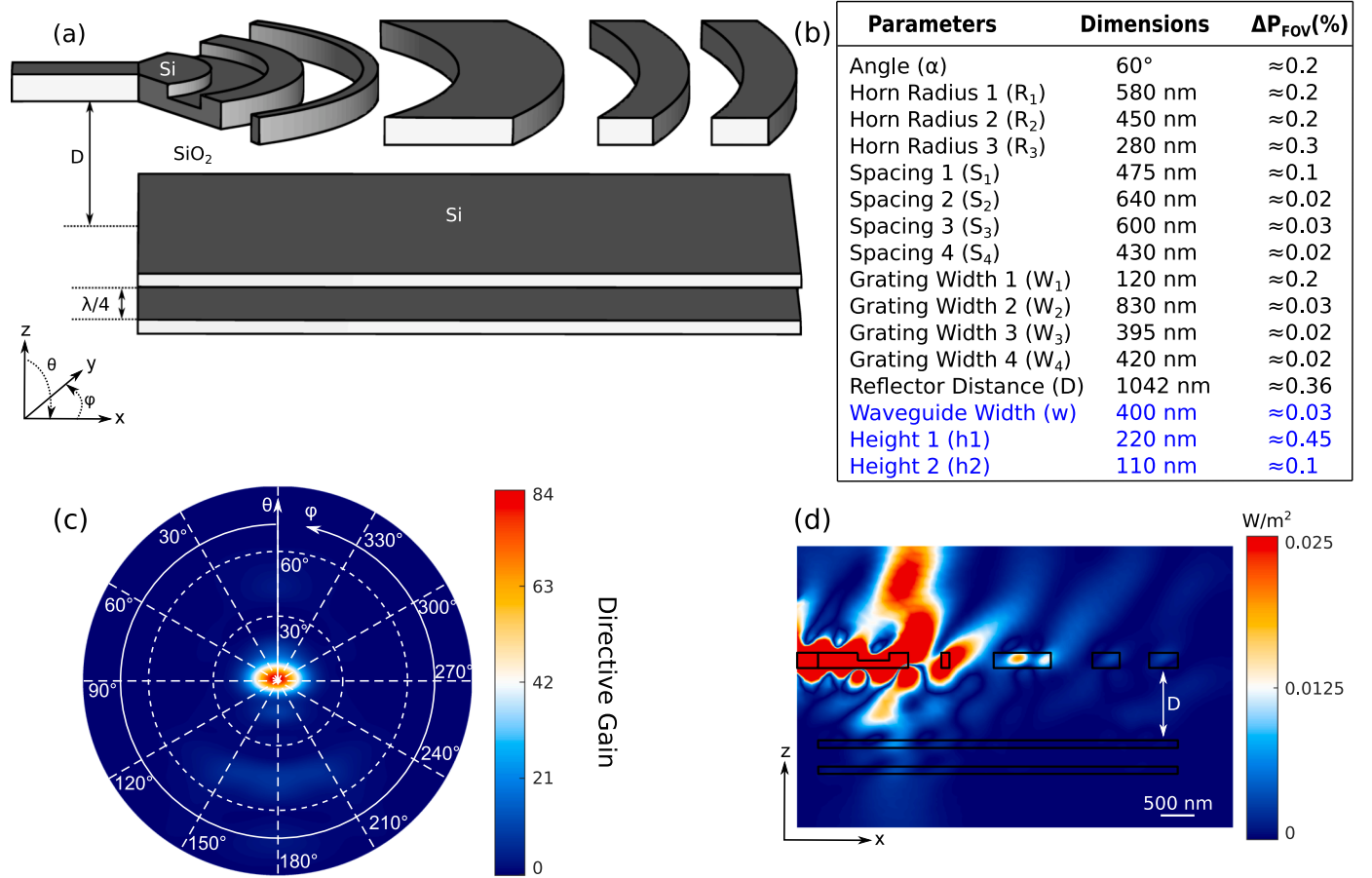


Fig. 3. (a) Schematic representation of the dielectric antenna with the Bragg reflector optimized for 1.55 μm , highlighting the parameters used in the optimization. (b) Design parameters obtained from the optimization process. (c) Calculated angular linear directive gain distribution of the antenna exhibiting a directivity of $D = 84$ at $\theta = 1^\circ$. (d) Calculated near-field distribution of the power flow for the optimized antenna in the xz -plane at $y = 0$.

where d is the size of the unit cell, which is 9 μm in this case and λ_n is the wavelength in the medium of propagation. Therefore, such an array configuration has a FOV that can be approximated to $6.8^\circ \times 6.8^\circ$ along θ_x and θ_y , respectively, with m propagating interference orders, where m is the largest value that satisfies $|m\lambda_n/d| < 2$. Thus, in our unit cell, we have 16 interference orders in each direction.

3. Results and discussion

We begin with the optimization of the first structure shown in Fig. 2a. It comprises an initial waveguide that guides light into the horn section with a partial etch followed by five circular gratings with a variable pitch. This gives twelve optimization parameters, as highlighted in the figure. The parameters include the angle (α), horn radius 1 (R_1), horn radius 2 (R_2), horn radius 3 (R_3), spacing 1 (S_1), spacing 2 (S_2), spacing 3 (S_3), spacing 4 (S_4), grating width 1 (W_1), grating width 2 (W_2), grating width 3 (W_3) and grating width 4 (W_4). The table in Fig. 2b highlights the values of these parameters for the optimized antenna, and the values in blue specify the fixed parameters for the excitation waveguide width (w), the full height (h_1), and partial etch height (h_2) of the antenna. The partial etch helps break the up-down symmetry of the antenna in order to have a higher upward radiation efficiency than the downward radiation efficiency, utilizing the constructive-destructive interference [40,41]. At 1.55 μm , the optimized antenna exhibits a linear directivity of 54 at an angle of $\theta = 0^\circ$ and $\varphi = 0^\circ$. For the aforementioned wavelength, the antenna demonstrates a half-power beam-width (HPBW) of $12.5^\circ \times 22.2^\circ$, as shown in Fig. 2c, representing the calculated directive gain distribution of the antenna. Fig. 2d shows the

near-field power distribution of the structure, which exhibits upward propagation of the power. Taking a look at the broadband efficiencies of this structure, at a wavelength of $\lambda = 1.55 \mu\text{m}$, this structure has an upward efficiency of 51%, downward efficiency of 39%, and reflection efficiency of 10% back to the waveguide (see Fig. 4a). Interestingly, Fig. 4c reveals that approximately 3.2% of the optical power is radiated into the FOV. Overall, the antenna structure has a compact footprint of approximately $5.2 \mu\text{m} \times 3.27 \mu\text{m}$ and the variable spacing between the gratings of different sizes helps improve the performance of this antenna. Additionally, the ΔP_{FOV} in Fig. 2b represents the sensitivity of each parameter with respect to the figure of merit, i.e., the radiation efficiency in the FOV. The sensitivity analysis is shown for $\pm 2^\circ$ for α and $\pm 10 \text{ nm}$ for all the other parameters, highlighting their tolerance to fabrication imperfections. It is evident from this analysis that α , h_1 , and h_2 are the most sensitive parameters, as they affect the footprint and diffraction efficiency of the antenna.

To further improve the upward efficiency and the power in FOV, we add an additional asymmetry by introducing a silicon-based Bragg reflector under the antenna structure. The reflector consists of two silicon mirrors with a width of $\lambda_{\text{Si}}/4$, that are separated by a distance of $\lambda_{\text{SiO}_2}/4$, where λ_{Si} and λ_{SiO_2} are the wavelengths in silicon and silicon-dioxide, respectively. The schematic of the structure is shown in Fig. 3a with one new optimization parameter, the reflector distance (D), in addition to the twelve parameters of the fundamental structure shown in Fig. 2a. The value of all the thirteen parameters for the newly optimized design along with the sensitivity of each parameter is shown in Fig. 3b. Again, the sensitivity analysis reflects the tolerance for $\pm 2^\circ$ for α , and $\pm 10 \text{ nm}$ for all the other parameters. At 1.55 μm , this structure

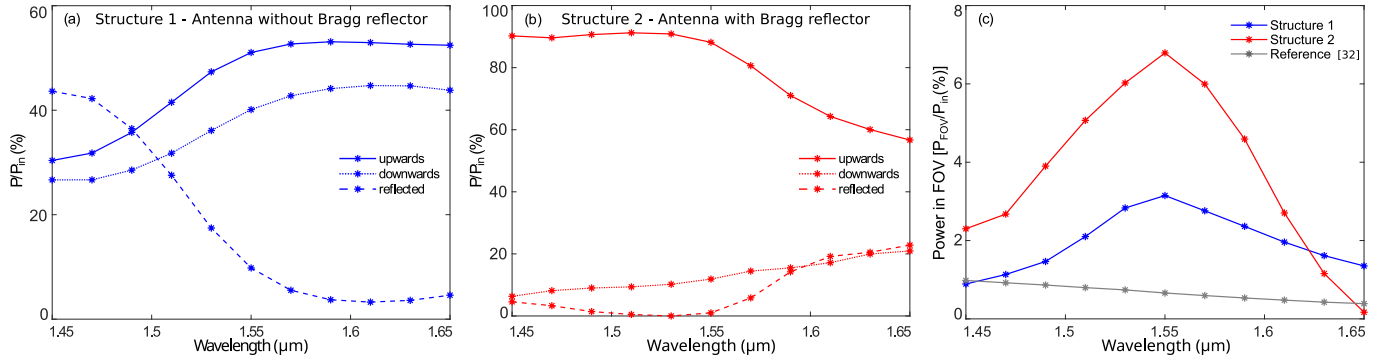


Fig. 4. Calculated optical radiation efficiencies of the optimized antenna (a) without and (b) with the Bragg reflector. (c) Calculated power in the FOV for both optimized antennas in comparison to the antenna presented in [32].

demonstrates a linear directivity of 84 along $\theta = 1^\circ$ and $\varphi = 0^\circ$, with an HPBW of $11.2^\circ \times 19.8^\circ$, as seen in Fig. 3c. This increased gain is attributed to the use of the simple reflector, which also becomes evident from the near-field distribution showing an increased upward propagation of the power (see Fig. 3d). This configuration now exhibits an upward efficiency of 88%, a downward efficiency of 11%, and a reflection efficiency of 1% (see Fig. 4b). In particular, 6.8% of the optical power is directed into the FOV, which is two times more than that of the fundamental antenna without the reflector. This antenna structure has a footprint of approximately $5.2 \mu\text{m} \times 3.3 \mu\text{m}$, similar to the initial structure.

To compare the two structures investigated in this work, we plot in Fig. 4a and b the calculated radiation efficiencies as a function of the wavelength. As it can be seen, both antennas maintain a good upward efficiency for a broad range of frequencies, making them both broadband antennas. Remarkably, the reflector produces not just an increased upward efficiency but also a significantly reduced reflection efficiency of 1% at the operational wavelength, as depicted by the dashed red curve in Fig. 4b. Additionally, Fig. 4c shows the optimized cost function, radiation efficiency in the FOV. We achieve a significant improvement in power concentration in the field of view (FOV) with our optimized antennas, outperforming the reference antenna (gray curve). The reference antenna's FOV radiation efficiency is calculated for the geometric dimensions provided in [32]. Our antenna without the Bragg reflector can concentrate around five times more power in the FOV compared to the reference antenna, while the antenna with the Bragg reflector can concentrate around ten times more power in the FOV. Additionally, as per the sensitivity analysis, our optimized antennas are robust to

fabrication imperfections, making them highly desirable.

Furthermore, the field from a single antenna can be employed for the calculation of the electromagnetic far-field radiation of the OPA as

$$\mathbf{E}_{\text{array}}(\theta, \varphi) = \mathbf{E}_{\text{antenna}}(\theta, \varphi) \text{AF}(\theta, \varphi), \quad (2)$$

where $\mathbf{E}_{\text{antenna}}(\theta, \varphi)$ is the far-field of a single antenna, $\text{AF}(\theta, \varphi)$ is the scalar function representing the array factor, $\mathbf{E}_{\text{array}}(\theta, \varphi)$ is the far-field of the OPA, θ is polar, and φ is the azimuthal angle of the far-field [1]. Such arrays are commonly used in beam steering, like in radar and LiDAR, and conventionally, the large-scale integration makes it possible to generate complex radiation patterns with high resolution. Our optimized antennas can also be employed in such a 2-D phased array setup for desired pattern generation. The Gerchberg-Saxton algorithm is employed for the pattern synthesis, which utilizes the near-field and far-field intensity distributions to iteratively determine the phase required by each radiating element to generate the desired far-field pattern (in this case, the UPB initials of Paderborn University) [42, 43]. As the far-field quantity is known, the inverse Fourier transform of this data acts as the initial condition for the algorithm. At any given iteration, the approximate far-field quantity produced by the algorithm is inverse Fourier transformed to provide the magnitude and phase in the near-field. But as the name suggests, the far-field pattern is controlled by the phase and not the amplitude. Therefore, a uniform amplitude distribution of unity is maintained, and the phases generated by the algorithm for producing the UPB initials are used. Fig. 5a and b show the simulated far-field patterns of the 64×64 array configurations of the optimized antenna without and with the Bragg reflector, respectively. In particular at $1.55 \mu\text{m}$, the OPA configurations without and with the

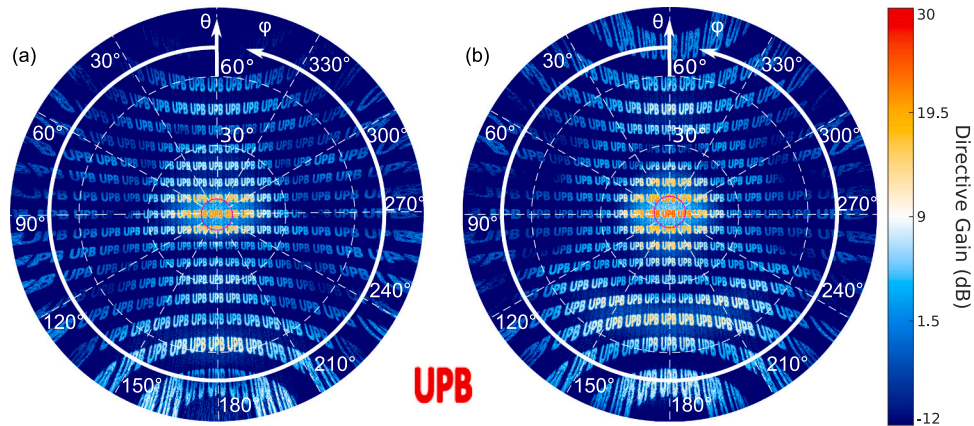


Fig. 5. Calculated far-field radiation patterns for a 64×64 phased array configuration with respect to the optical antenna (a) without and (b) with the Bragg reflector to generate the Paderborn University logo (UPB) at $1.55 \mu\text{m}$. The original logo used in the process is shown in the middle. The pink circle highlights the FOV region.

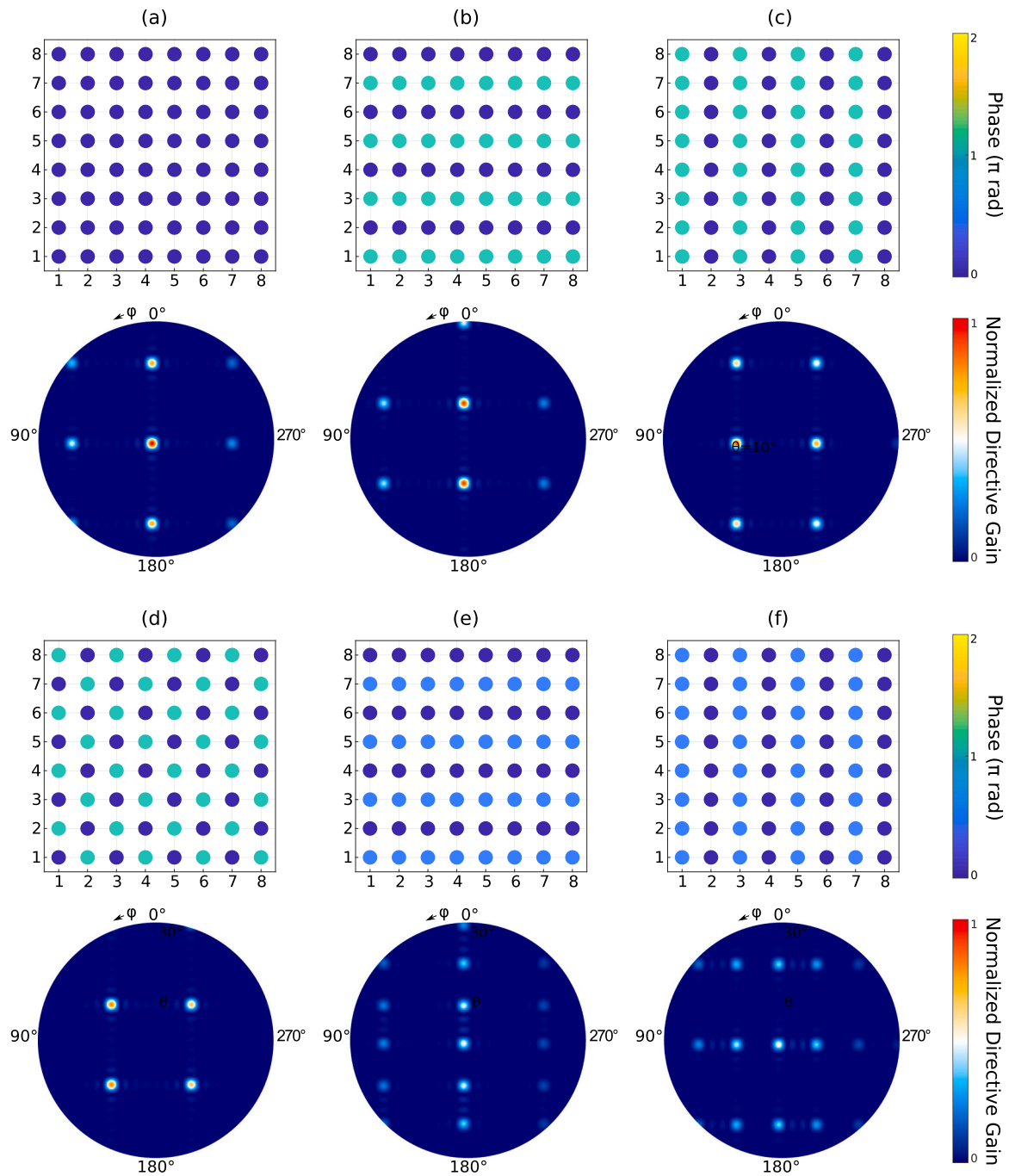


Fig. 6. Demonstration of beam steering and beamforming with an 8×8 array configuration of the antenna with the Bragg reflector at $1.55 \mu\text{m}$. (a) Phase distribution and simulated linear far-field radiation pattern of a uniform phased array. (b–f) Phase distribution and the simulated linear far-field radiation pattern for the main lobe to be (b) shifted vertically, (c) shifted horizontally, (d) shifted diagonally, (e) split vertically, and (f) split horizontally, respectively.

Bragg reflector possess a side lobe level of -2.5 dB and -2.7 dB , respectively. The pink circle highlights the region of the FOV. In agreement with our optimization results, it can be seen in Fig. 5b that the antenna with the reflector generates more power inside the pink circle, manifested in the brighter red of the radiation pattern in comparison to the antenna without the reflector (Fig. 5a). The original UPB logo used for the pattern generation is shown in the middle, and as suggested before, 16 interference orders correspond to 16 repetitions of the logo in each direction.

Finally, we show the possibility of beam steering and preliminary beamforming with our antennas. For this purpose, we considered an 8×8 array configuration of the antenna with the Bragg reflector. Fig. 6

shows the different phase configurations and the correspondingly generated far-field radiation patterns. In order to have a better visualization of the steering effect, the far-field patterns only show a small region of the polar angle, i.e., up to $\theta = 10^\circ$. Fig. 6a presents the initial case, where no phase distribution is applied to the uniformly excited array, demonstrating a directivity of 37.3 dB . All radiation patterns in Fig. 6 are normalized to this directivity. An alternating phase distribution of 0 and π along the rows or columns of the array, as shown in Fig. 6b and c, allows the beam to be steered along the vertical or horizontal direction, respectively. In particular, the vertical steering results in a directivity drop of 0.4 dB , and the horizontal steering case has a drop of 0.7 dB . Similarly, using this alternating phase distribution along

Table 1
Comparison with different antennas.

Design	Footprint	η_{up}	θ
[32]	3.5 $\mu\text{m} \times$ 2.8 μm	51%	15°
[24]	5 $\mu\text{m} \times$ 2 μm	51%	7.4°
[44]	5.5 $\mu\text{m} \times$ 2.5 μm	71%	6°
[25]	5.1 $\mu\text{m} \times$ 2 μm	35%	9°
This work (Structure 1)	5.2 $\mu\text{m} \times$ 3.27 μm	51%	0°
This work (Structure 2)	5.2 $\mu\text{m} \times$ 3.3 μm	88%	1°

the rows and columns will shift the position of the beam in both the horizontal and vertical direction, essentially steering the beam along a diagonal, as shown in Fig. 6d, with a directivity drop of 1 dB. Furthermore, the tightly focused main lobe can also be split vertically or horizontally by using an alternating phase distribution of 0 and $\pi/2$ along the rows or columns, as shown in Fig. 6e and f, respectively. The splitting of the beam results in the power being divided between the two new beams, thus demonstrating ~ 3 dB drop in the directivity. Therefore, the presented antenna can be efficiently utilized in applications that require beam steering.

Finally, in Table 1, we compare our proposed antennas with other antennas suitable for OPAs with respect to upward radiation efficiency (η_{up}) and their main lobe emission angle (θ) for the wavelength of 1.55 μm . Our antennas have a comparable footprint with near-vertical emission. Moreover, Structure 2 has a significantly higher upward radiation efficiency with the ability to efficiently concentrate power in the FOV. Therefore, we believe that our proposed radiating elements offer a viable solution to applications that demand highly directive phased arrays.

4. Conclusion

The dielectric antennas presented in this work were optimized to direct more power into the array FOV sized $6.8^\circ \times 6.8^\circ$ at 1.55 μm . Our first optimized antenna demonstrates an upward efficiency of 51%, and 3.2% of the optical power is directed into the FOV. Our second antenna, empowered by the use of a simple yet efficient Bragg reflector, reveals an upward efficiency of approximately 90% with 6.8% of the optical power being directed into the FOV, which is ten times more in comparison to the reference antenna [32]. This increased efficiency is achieved with the use of a silicon Bragg reflector. Furthermore, by manipulating the phase distribution of all the antennas comprising the 2-D array, we show the possibility of beam steering and beamforming. We anticipate that our robust optimized antennas can be easily fabricated and utilized for enhancing the performance of LiDAR and OPAs used in different applications.

Declaration of Competing Interest

The authors declare the following financial interests/personal relationships which may be considered as potential competing interests: Jens Förstner reports financial support was provided by Deutsche Forschungsgemeinschaft. J.C. Scheytt reports financial support was provided by Ministry of Culture and Science of the State of North Rhine-Westphalia.

Data availability

Data underlying the results presented in this paper are publicly available. <https://doi.org/10.5281/zenodo.10044122>.

Acknowledgments

The work was funded by the Ministry of Culture and Science of the state of North Rhine-Westphalia via the PhoQC project. Additionally, the

authors gratefully acknowledge financial support from the Deutsche Forschungsgemeinschaft (DFG) via TRR142 projects C05 and B06 and the computing time support provided by the Paderborn Center for Parallel Computing (PC²).

References

- [1] C.A. Balanis. *Antenna Theory: Analysis and Design*, John Wiley & Sons, 2015.
- [2] F. Ashtiani, F. Aflatouni, N \times N optical phased array with 2N phase shifters, *Opt. Express* 27 (19) (2019) 27183–27190.
- [3] A.J. Fenn, D.H. Temme, W.P. Delaney, W.E. Courtney, The development of phased-array radar technology, *Linc. Lab. J.* 12 (2) (2000) 321–340.
- [4] J. Sun, E. Timurdogan, A. Yaacobi, E.S. Hosseini, M.R. Watts, Large-scale nanophotonic phased array, *Nature* 493 (7431) (2013) 195–199.
- [5] W.S. Rabinovich, P.G. Goetz, M. Pruessner, R. Mahon, M.S. Ferraro, D. Park, E. Fleet, and M.J. DePrenger, Free space optical communication link using a silicon photonic optical phased array, In *Free-Space Laser Communication and Atmospheric Propagation XXVII*, vol. 9354. International Society for Optics and Photonics, 2015, 93540B.
- [6] W.M. Neubert, K.H. Kudielka, W.R. Leeb, A.L. Scholtz, Experimental demonstration of an optical phased array antenna for laser space communications, *Appl. Opt.* 33 (18) (1994) 3820–3830.
- [7] P.-A. Blanche, L. LaComb, Y. Wang, M.C. Wu, Diffraction-based optical switching with MEMS, *Appl. Sci.* 7 (4) (2017) 411, <https://doi.org/10.3390/app7040411>.
- [8] J. Zhou, J. Sun, A. Yaacobi, C.V. Poulton, M.R. Watts, Design of 3D hologram emitting optical phased arrays, In *Integrated Photonics Research, Silicon and Nanophotonics*, Optical Society of America IT4A-7. (2015).
- [9] C.V. Poulton, M.J. Byrd, P. Russo, E. Timurdogan, M. Khandaker, D. Vermeulen, M. R. Watts, Long-range LiDAR and free-space data communication with high-performance optical phased arrays, *IEEE J. Sel. Top. Quantum Electron.* 25 (5) (2019) 1–8.
- [10] J. Levinson, J. Askeland, J. Becker, J. Dolson, D. Held, S. Kammel, J.Z. Kolter, D. Langer, O. Pink, V. Pratt et al., Towards fully autonomous driving: Systems and algorithms, In *2011 IEEE intelligent vehicles symposium (IV)*. IEEE, 2011, 163–168.
- [11] C.V. Poulton, A. Yaacobi, D.B. Cole, M.J. Byrd, M. Raval, D. Vermeulen, M. R. Watts, Coherent solid-state LiDAR with silicon photonic optical phased arrays, *Opt. Lett.* 42 (20) (2017) 4091–4094.
- [12] P. Bhargava, T. Kim, C.V. Poulton, J. Notaros, A. Yaacobi, E. Timurdogan, C. Baiocco, N. Fahrenkopf, S. Kruger, T. Ngai, et al., Fully integrated coherent LiDAR in 3D-integrated silicon photonics/65nm CMOS, in: *2019 Symposium on VLSI Circuits*, IEEE, 2019, pp. C262–C263.
- [13] W. Guo, P.R. Binetti, C. Althouse, M.L. Mašanović, H.P. Ambrosius, L.A. Johansson, L.A. Coldren, Two-dimensional optical beam steering with InP-based photonic integrated circuits, *IEEE J. Sel. Top. Quantum Electron.* 19 (4) (2013) 6100212.
- [14] C. Sun, L. Yang, B. Li, W. Shi, H. Wang, Z. Chen, X. Nie, S. Deng, N. Ding, A. Zhang, Parallel emitted silicon nitride nanophotonic phased arrays for two-dimensional beam steering, *Opt. Lett.* 46 (22) (2021) 5699–5702.
- [15] J. Hulme, J. Doylend, M. Heck, J. Peters, M. Davenport, J. Bovington, L. Coldren, J. Bowers, Fully integrated hybrid silicon two dimensional beam scanner, *Opt. Express* 23 (5) (2015) 5861–5874.
- [16] J. Doylend, M. Heck, J. Bovington, J. Peters, M. Davenport, L. Coldren, J. Bowers, Hybrid III/V silicon photonic source with integrated 1D free-space beam steering, *Opt. Lett.* 37 (20) (2012) 4257–4259.
- [17] D. Resler, D. Hobbs, R. Sharp, L. Friedman, T. Dorschner, High-efficiency liquid-crystal optical phased-array beam steering, *Opt. Lett.* 21 (9) (1996) 689–691.
- [18] P.F. McManamon, T.A. Dorschner, D.L. Corkum, L.J. Friedman, D.S. Hobbs, M. Holz, S. Liberman, H.Q. Nguyen, D.P. Resler, R.C. Sharp, et al., Optical phased array technology, *Proc. IEEE* 84 (2) (1996) 268–298.
- [19] S. Chung, H. Abediasl, H. Hashemi, A monolithically integrated large-scale optical phased array in silicon-on-insulator CMOS, *IEEE J. Solid-State Circuits* 53 (1) (2017) 275–296.
- [20] H. Abediasl, H. Hashemi, Monolithic optical phased-array transceiver in a standard SOI CMOS process, *Opt. Express* 23 (5) (2015) 6509–6519.
- [21] K. Van Acoleyen, H. Rogier, R. Baets, Two-dimensional optical phased array antenna on silicon-on-insulator, *Opt. Express* 18 (13) (2010) 13655–13660.
- [22] K. Van Acoleyen, W. Bogaerts, J. Jägerská, N. LeThomas, R. Houdré, R. Baets, Off-chip beam steering with a one-dimensional optical phased array on silicon-on-insulator, *Opt. Lett.* 34 (9) (2009) 1477–1479.
- [23] J.K. Doylend, M. Heck, J.T. Bovington, J.D. Peters, L. Coldren, J. Bowers, Two-dimensional free-space beam steering with an optical phased array on silicon-on-insulator, *Opt. Express* 19 (22) (2011) 21595–21604.
- [24] R. Fatemi, A. Khachaturian, A. Hajimiri, A nonuniform sparse 2-D large-FOV optical phased array with a low-power PWM drive, *IEEE J. Solid-State Circuits* 54 (5) (2019) 1200–1215.
- [25] R. Fatemi, P.P. Khial, A. Khachaturian, A. Hajimiri, Breaking FOV-aperture trade-off with multi-mode nano-photonic antennas, *IEEE J. Sel. Top. Quantum Electron.* 27 (1) (2020) 1–14.
- [26] M.R. Kossey, C. Rizk, A.C. Foster, End-fire silicon optical phased array with half-wavelength spacing, *APL Photon.* 3 (1) (2018).
- [27] C.V. Poulton, M.J. Byrd, M. Raval, Z. Su, N. Li, E. Timurdogan, D. Coolbaugh, D. Vermeulen, M.R. Watts, Large-scale silicon nitride nanophotonic phased arrays at infrared and visible wavelengths, *Opt. Lett.* 42 (1) (2017) 21–24.

- [28] B. Abiri, R. Fatemi, A. Hajimiri, A 1-D heterodyne lens-free optical phased array camera with reference phase shifting, *IEEE Photon. J.* 10 (5) (2018) 1–12.
- [29] S.A. Miller, C.T. Phare, Y.-C. Chang, X. Ji, O.A.J. Gordillo, A. Mohanty, S. P. Roberts, M.C. Shin, B. Stern, M. Zadka, et al., 512-element actively steered silicon phased array for low-power LiDAR. *CLEO: Science and Innovations, Optica Publishing Group*, 2018. JTh5C-2.
- [30] S.T. Ilie, T.D. Bucio, T. Rutirawut, L. Mastronardi, I. Skandalos, H. Chong, F. Y. Gardes, Silicon-rich silicon nitride CMOS platform for integrated optical phased arrays. In *Smart Photonic and Optoelectronic Integrated Circuits XXIII*, vol. 11690, SPIE, 2021, pp. 13–21.
- [31] D. Benediković, Q. Liu, A. Sánchez-Postigo, A. Atieh, T. Smy, P. Cheben, W.N. Ye, Circular optical phased array with large steering range and high resolution, *Sensors* 22 (16) (2022) 6135.
- [32] J. Sun, E. Timurdogan, A. Yaacobi, Z. Su, E.S. Hosseini, D.B. Cole, M.R. Watts, Large-scale silicon photonic circuits for optical phased arrays, *IEEE J. Sel. Top. Quantum Electron.* 20 (4) (2013) 264–278.
- [33] H. Farheen, L.-Y. Yan, V. Quiring, C. Eigner, T. Zentgraf, S. Linden, J. Förstner, V. Myroshnychenko, Broadband optical Ta₂O₅ antennas for directional emission of light, *Opt. Express* 30 (11) (2022) 19288–19299.
- [34] H. Farheen, T. Leuteritz, S. Linden, V. Myroshnychenko, J. Förstner, Optimization of optical waveguide antennas for directive emission of light, *JOSA B* 39 (1) (2022) 83–91.
- [35] T. Leuteritz, H. Farheen, S. Qiao, F. Spreyer, C. Schlickriede, T. Zentgraf, V. Myroshnychenko, J. Förstner, S. Linden, Dielectric travelling wave antennas for directional light emission, *Opt. Express* 29 (10) (2021) 14694–14704.
- [36] Dassault Systèmes CST Studio Suite, (<https://www.cst.com>). 2023.
- [37] A. Taflov, S.C. Hagness, M. Picket-May, Computational electromagnetics: The finite-difference time-domain method, *The Electrical Engineering Handbook* 3 (2005).
- [38] P. Cheben, R. Halir, J.H. Schmid, H.A. Atwater, D.R. Smith, Subwavelength integrated photonics, *Nature* 560 (7720) (2018) 565–572.
- [39] C. Palmer. *Diffraction Grating Handbook*, MKS instruments, Inc, New York, NY, USA, 2020.
- [40] G. Roelkens, D. Van Thourhout, R. Baets, High efficiency silicon-on-insulator grating coupler based on a poly-silicon overlay, *Opt. Express* 14 (24) (2006) 11622–11630.
- [41] M. Fan, M.A. Popović, F.X. Kärtner, High directivity vertical fiber-to-chip coupler with anisotropically radiating grating teeth. *Conference on Lasers and Electro-Optics*, Optica Publishing Group, 2007. CTuDD3.
- [42] R.W. Gerchberg, A practical algorithm for the determination of plane from image and diffraction pictures, *Optik* 35 (2) (1972) 237–246.
- [43] J.R. Fienup, Reconstruction of an object from the modulus of its fourier transform, *Opt. Lett.* 3 (1) (1978) 27–29.
- [44] Q. Liu, D. Benedikovic, T. Smy, A. Atieh, P. Cheben, W.N. Ye, Circular optical phased arrays with radial nano-antennas, *Nanomaterials* 12 (11) (2022) 1938, <https://doi.org/10.3390/nano12111938>.